

Minerva Access is the Institutional Repository of The University of Melbourne

Author/s:

Pfaff, M;Müller, P;Bockstaller, P;Müller, E;Subbiah, J;Wong, WWH;Klein, MFG;Kiersnowski, A;Puniredd, SR;Pisula, W;Colsmann, A;Gerthsen, D;Jones, DJ

Title:

Bulk heterojunction nanomorphology of fluorenyl hexa- peri -hexabenzocoronene-fullerene blend films

Date:

2013-11-27

Citation:

Pfaff, M., Müller, P., Bockstaller, P., Müller, E., Subbiah, J., Wong, W. W. H., Klein, M. F. G., Kiersnowski, A., Puniredd, S. R., Pisula, W., Colsmann, A., Gerthsen, D. & Jones, D. J. (2013). Bulk heterojunction nanomorphology of fluorenyl hexa- peri -hexabenzocoronene-fullerene blend films. *ACS Applied Materials and Interfaces*, 5 (22), pp.11554-11562. <https://doi.org/10.1021/am4044085>.

Persistent Link:

<https://hdl.handle.net/11343/220200>

Bulk heterojunction nanomorphology of fluorenyl hexa-*peri*-hexabenzocoronene-fullerene blend films

Marina Pfaff,^{*1,2} Philipp Müller,^{1,2} Pascal Bockstaller,¹ Erich Müller,¹ Jegadesan Subbiah,³
Wallace W. H. Wong,³ Michael F. G. Klein,⁴ Wojciech Pisula,⁵ Adam Kiersnowski,^{5,6}
Sreenivasa Reddy Puniredd,^{5,7} Wojciech Pisula,⁵ Uli Lemmer,^{2,4} Alexander Colsmann,⁴
Dagmar Gerthsen^{1,2}, David J. Jones^{#,3}

¹ Laboratory for Electron Microscopy, Karlsruhe Institute of Technology (KIT), Engesserstr. 7,
76131 Karlsruhe, Germany.

² Center for Functional Nanostructures (CFN), Karlsruhe Institute of Technology (KIT)

³ School of Chemistry, Bio21 Institute, University of Melbourne, 30 Flemington Road,
Parkville, Victoria 3010, Australia.

⁴ Light Technology Institute, Karlsruhe Institute of Technology (KIT), Engesserstr.13, 76131
Karlsruhe, Germany.

⁵ Max Planck Institute for Polymer Research, Ackermannweg 10, 55128 Mainz, Germany.

⁶ Wroclaw University of Technology, Polymer Engineering and Technology Division,
Wybrzeze Wyspianskiego 27, 50-370 Wroclaw, Poland

⁷ Present address: Institute of Materials Research and Engineering, A*Star, 3 Research Link,
Singapore, 117602

KEYWORDS (5-7 keywords): Organic solar cells, nanomorphology, hexabenzocoronene, electron microscopy, dark-field imaging, EFTEM, electron tomography

AUTHOR INFORMATION

***Submitting Author**

Marina Pfaff

e-mail: marina.pfaff@kit.edu

phone: +49 721 6084 8682

fax: +49 721 60843721

mailing address:

Laboratorium für Elektronenmikroskopie

Engesserstr. 7, Geb. 30.22, R.228

76131 Karlsruhe

Germany

#Corresponding author

David D. Jones

...

ABSTRACT

In this study the nanomorphology of fluorenyl hexa-*peri*-hexabenzocoronene: [6,6]-phenyl C₆₁-butyric acid methyl ester FHBC:PC₆₁BM absorber layers of organic solar cells was investigated. Different electron microscopical techniques, atomic force microscopy and grazing incidence wide-angle X-ray scattering were applied for a comprehensive nanomorphology analysis. The development of the nanomorphology upon sample annealing and the associated change of the device performance were investigated. It was shown that the annealing process induces a phase separation leading to a bulk heterojunction structure. Due to π - π stacking the FHBC molecules assemble into columnar stacks, which are already present before annealing. While the non-annealed sample consists of a mixture of homogeneously distributed PC₆₁BM molecules and FHBC stacks with a preferential in-plane stack orientation, crystalline FHBC precipitates occur in the annealed samples. These crystals, which consist of hexagonal arranged FHBC stacks, grow with increased annealing time. They are distributed homogeneously over the whole volume of the absorber layer as revealed by electron tomography. The FHBC stacks - whether in the two phase mixture or in the pure crystalline precipitates - exhibit an edge-on orientation, according to results from grazing incidence wide-angle X-ray scattering (GIWAXS), dark-field transmission electron microscopy (DF TEM) imaging and selective area electron diffraction (SAED). The best solar cell efficiencies were obtained after 20 and 40 s sample annealing. These annealing times provide an optimized degree of phase separation between donor and acceptor material.

Introduction

Bulk heterojunction (BHJ) organic solar cells (OSC) are a promising photovoltaic devices that can be manufactured at low-cost using roll-to-roll printing methods.¹ The basic operation of BHJ OSCs relies on absorption of light in a blend of donor and acceptor materials. The photo-generated charges form excited states, before being spatially separated and subsequently collected at the electrodes.^{2, 3} To optimize the BHJ morphology and hence the device performance, it is crucial to gain as much knowledge as possible about the underlying mechanism of device operation. There are many aspects of a BHJ that can affect the overall device performance. These include the individual properties of the materials, such as spectral absorption and charge transport, as well as the compatibility of materials, such as frontier orbital energy matching and interface formation. In detailed device studies, often the most elusive parameter that affects the device performance is the nanomorphology of the donor-acceptor blends.

Several techniques are available for nanomorphology characterization of BHJ OSCs which contain donor-acceptor blends. Most commonly used is atomic force microscopy (AFM) which provides information on the surface topography but not on the bulk properties of the film. The volume properties of the absorber layers can be studied by TEM which comprises several imaging modes to probe different sample properties. While bright-field (BF) TEM is the most common mode to investigate the morphology of BHJ solar cells,⁴⁻⁷ DF TEM has been rarely used. This is due to the fact that polymers with crystalline structure are usually sensitive to electron irradiation and relatively long exposure times are necessary to record DF TEM images. Only few examples for DF imaging of polymer samples can be found in literature.^{8, 9} High-resolution TEM (HRTEM) is used to directly image the crystalline structure but its application is restricted by the electron-beam sensitivity of organic materials. Nevertheless, numerous examples of HRTEM investigations of polymers or organic molecules can be found in literature as summarized Martin et al.¹⁰ Electron energy loss spectroscopy (EELS) and energy-filtered TEM (EFTEM) have been used by several groups to distinguish acceptor and donor domains in BHJ OSCs. The distinction is based on the fact that the plasmon energies of the examined absorber materials differ.¹¹⁻¹³ Low-energy high-angle annular dark-field scanning TEM (HAADF STEM), a technique with sensitive material contrast, was applied for imaging the nanomorphology of poly(3-hexylthiophene):[6,6]-phenyl C₆₁-butyric acid methyl ester (P3HT:PC₆₁BM) blends.¹⁴ All standard TEM-based techniques only provide a two-dimensional projection of the examined volume. This limitation can be overcome by TEM tomography which facilitates the reconstruction of the three-dimensional (3D) sample structure. Several

examples of 3D reconstructions of the nanomorphology of OSC absorber layers can be found in the literature.¹⁵⁻¹⁸

In our previous studies, FHBC was employed as electron donor material in BHJ OSCs.¹⁹ Hexa-*peri*-hexabenzocoronene (HBC) is a discotic polycyclic aromatic hydrocarbon with well-known liquid crystalline properties as a result of strong π - π intermolecular association between the molecules.¹⁹ The columnar π - π stacking results in high intrinsic charge transport properties making HBC materials attractive candidates for semi-conducting applications.¹⁹ While photovoltaic response of HBC containing devices was first demonstrated in 2001,²⁰ the introduction of fluorene substituents on the HBC molecule resulted in a material that showed a promising device performance in combination with the fullerene electron acceptor PC₆₁BM.¹⁹ Despite the restricted spectral absorption of this FHBC material with absorption onset at 450 nm, power conversion efficiencies (PCEs) of up to 1.5 % were recorded for these FHBC:PC₆₁BM devices with a maximum external quantum efficiency of 40 % at 400 nm.¹⁹ Perhaps, the most interesting aspect of the device characteristics was the high fill factor (FF) of up to 65 %. The high FF value indicated that the transport of holes and electrons through the BHJ film is well-balanced as was confirmed in charge mobility measurements.^{19, 21} The charge transport in BHJ films is determined by the intrinsic mobility of the individual donor and acceptor components as well as the nanomorphology created from the phase separation of the two materials. From our previous work, phase separation between the FHBC and PC₆₁BM materials was evident from the surface topology of the blend films in AFM experiments.¹⁹ Furthermore the crystalline structure of pure FHBC was revealed by 2D-wide-angle X-ray scattering (2D-WAXS).¹⁹ The results of this study are summarized in Fig. 1. Due to π - π stacking of planar aromatic FHBC molecules, self-assembly into columnar stacks occurs as indicated in Fig. 1b with a distance of 0.35 nm between single FHBC molecules. The columns can assemble in a hexagonal arrangement, with a plane distance between stacks of 2.15 nm (denoted with *d* in Fig. 1c).

In this study, various electron microscopic techniques, AFM and GIWAXS were applied to study the nanomorphology of FHBC:PC₆₁BM blends before and after annealing. Direct evidence for phase separation was obtained and the assembly of FHBC within the blends is revealed. Good correlation was found between the thermal treatment of the blend films, nanomorphology and BHJ device performance.

Experimental Results

To thoroughly investigate the nanomorphology of FHBC:PC₆₁BM blends after different annealing times and to correlate the results with the device performance, solar cell devices and BHJ absorber layers with identical processing parameters and annealing treatments were fabricated. The presentation of the results is accordingly divided into two parts. In the first part the photovoltaic performance of the solar cell devices is presented. The focus of the second part lies on the nanomorphology investigation.

Photovoltaic Performance

The BHJ solar cells were fabricated using FHBC donor and PC₆₁BM acceptor molecules. A schematic diagram of the solar cell with a state-of-the-art device architecture is shown in Fig. 2a. On top of a structured indium tin oxide (ITO) coated glass slide a 25 nm thin layer of poly(3,4-ethylenedioxythiophene):poly(styrenesulfonate) (PEDOT:PSS) is deposited. The subsequently deposited 75 nm active layer comprises FHBC and PC₆₁BM (1:2 by wt.). A 10 nm titanium suboxide (TiO_x) layer and a 100 nm aluminum layer serve as top electrode. (see experimental section for details on device fabrication). The J-V characteristics of the devices under illumination after different annealing times are shown in Fig. 2b and the respective photovoltaic key performance data are summarized in Table 1. The FHBC:PC₆₁BM devices annealed for 20 s and 40 s at 150 °C showed the best device performance with PCEs of between 1.3 % and 1.4 %, respectively. The devices annealed for 0, 60 and 120 s exhibit a decreased device performance due to the moderate short circuit current (J_{sc}) and FF. These results are in agreement with those reported previously.¹⁹ With the device results confirmed, the nanomorphology of FHBC:PC₆₁BM blend films were examined.

Nanomorphology

Several electron microscopic techniques (BF TEM and DF TEM, SAED, EFTEM, TEM tomography), AFM and GIWAXS were applied to unravel the complex nanomorphology of the FHBC:PC₆₁BM absorber layers and the development of the nanomorphology with increasing annealing time.

Fig. 3 presents the results for the non-annealed sample. An AFM topography image is presented in Fig. 3a, which reveals depressions with a depth of about 10 nm. The depressions are surrounded by elongated structures (marked with black dashed lines). Additional height

variations are visible on larger scale, which can be attributed to layer thickness fluctuations. Examples for a higher and a deeper sample region are encircled in Fig. 3a.

To analyze the crystalline structure of the sample, SAED patterns were recorded at 200 keV in a transmission electron microscope. Pure FHBC and PC₆₁BM reference samples were additionally examined (data not shown here) to identify the FHBC and PC₆₁BM reflections. FHBC is characterized by two relatively sharp reflection rings which can be assigned to a real space distance of 0.35 nm. The inner ring corresponds to the π - π stacking distance displayed in Fig. 1. The outer ring at $(0.175 \text{ nm})^{-1}$ is the second order of the inner ring. The reflection rings of pure PC₆₁BM are broad and can be assigned to 0.46, 0.31 and 0.21 nm distances which agree with the results of other groups^{22, 23}. A diffraction pattern of the non-annealed FHBC:PC₆₁BM layer is presented in Fig. 3b and the according radial intensity linescan in Fig. 3c. The diffraction pattern shows three diffuse PC₆₁BM rings with a weak intensity of the two outer rings. One strong and relatively sharp FHBC ring (marked in Fig. 3b) is observed while the second ring at $(0.175 \text{ nm})^{-1}$ is barely recognizable. The high intensity of the inner ring indicates that FHBC stacks are already present in the non-annealed sample. The absence of further reflections suggests a preferential alignment of the stack axes parallel to the layer which will be denoted as in-plane stack orientation in the following. Moreover, the inner ring intensity changes azimuthally which is indicative for an inhomogeneous in-plane distribution of FHBC stack orientations. For example, the intensity is higher in the upper left and upper right ring segment. To study the origin of the anisotropy of the FHBC ring, dark-field (DF) TEM images were taken with the positions of the aperture indicated by the dashed circles in Fig. 3b. Accordingly, mainly electrons from these specific segments of the FHBC ring contribute to the images. The resulting DF TEM micrographs for the two aperture positions are presented in Fig. 3d and e which show bright and dark regions with a size of a few 100 nm. The displacement of the aperture position leads to images with essentially complementary contrast. Exemplarily, one grain is marked in both DF TEM images, which appears bright in Fig. 3d and dark in Fig. 3e. This clearly indicates a preferential in-plane alignment of FHBC stacks, i.e. a texture, in regions with a few 100 nm size. A BF TEM image taken at the same sample position as Figs. 3d,e is presented in Fig. 3f. None of the large-scale structures of the DF TEM images are visible here, only small-scale structures prevail. The small bright regions can be correlated with regions of smaller sample thickness due to small-size depression which are observed in the AFM image (Fig. 3a).

Fig. 4 presents results for the sample annealed for 120 s at 150 °C. The nanomorphology of this sample is representative for all annealed samples. The AFM topography image in Fig. 4a

shows depressions at the surface with sizes which do not depend on the annealing time. Again, elongated structures surrounding the depressions are visible (marked with black dashed lines). In contrast, the large-scale thickness variations disappear almost completely due to the annealing process (note the different height scale of the two AFM images Fig. 3a and Fig. 4a).

In Fig. 4b and c a diffraction pattern and the corresponding radial intensity linescan are shown. Azimuthal intensity variations along the FHBC reflection ring are not observed. However, this does not exclude a preferential FHBC stack alignment because the SAED pattern was taken from a relatively large area, which may contain differently textured grains. Grains with preferentially aligned FHBC stacks are indeed still present as demonstrated by the DF TEM image Fig. 4d which was taken with the aperture position marked by d) in Fig. 4b. In addition, small bright regions with a size of a few 10 nm appear in Fig. 4d which are absent in the non-annealed samples. The high intensity of these regions suggests crystalline FHBC precipitates. The presence of crystalline FHBC is supported by the high intensity and small width of the FHBC ring in the diffraction pattern (Figs. 4b,c) The DF TEM image in Fig. 4e was taken with the aperture position shifted to the PC₆₁BM ring. A smaller aperture was chosen to exclude any contribution from FHBC and select only the intensity of the PC₆₁BM ring (see Fig. 4b aperture position e). The PC₆₁BM-sensitive DF TEM image shows a homogeneous intensity apart from the interspersed dark regions which can be assigned to the FHBC precipitates. Fig. 4d suggests that the PC₆₁BM distribution is homogeneous in the phase surrounding the FHBC precipitates. We conclude that a two-phase structure is present after annealing which consists of a FHBC:PC₆₁BM mixture and crystalline FHBC precipitates. Within the FHBC:PC₆₁BM mixture, grains are formed with a preferential alignment of FHBC stacks. The BF TEM image Fig. 4f shows small bright regions which can be correlated with regions of smaller sample thickness. However, the grain structure with preferentially oriented FHBC stacks cannot be visualized by BF TEM.

By comparing FHBC-sensitive DF TEM images of samples with different annealing times (Fig. 5), it becomes apparent that the crystalline FHBC precipitates are formed quickly already after only 20 s annealing time. If the annealing time is increased, the FHBC crystallites grow slightly, but the large-scale texture of FHBC stacks in the FHBC:PC₆₁BM mixture remains.

To analyze the development of the morphology at even longer annealing times, a sample annealed for 5 min was investigated (not shown here). The size of the FHBC-rich crystallites does not increase significantly as compared to the sample annealed for 120 s, but large PC₆₁BM crystals with sizes of a few microns appear which are surrounded by an FHBC-rich region.

A HRTEM image of the sample annealed for 60 s is presented in Fig. 6 which is representative for all annealed samples. Lattice fringes are observed in the regions marked by dashed lines in Fig. 6a, which are indicative for a crystalline structure. Fig. 6b shows the crystalline region in the dashed square with a higher magnification. To determine the distance of the lattice fringes the Fourier transform of this image was calculated (Fig. 6c). Two bright spots are visible in addition to the zero-order beam, which correspond to a lattice fringe distance of 2.15 ± 0.15 nm. This distance can be correlated to the lattice plane distance in the hexagonal arrangement of the pure FHBC stacks (Fig. 1c). A detailed analysis will follow in the discussion section.

To confirm the interpretation of the images in Fig. 4 with respect to the distribution of PC₆₁BM and FHBC, EFTEM was applied. For this purpose, reference EEL spectra of pure FHBC and pure PC₆₁BM were recorded which are presented in Fig. 7d. The maxima of the plasmon peaks are clearly different for the two materials (FHBC at an energy loss of 22.5 eV, PC₆₁BM at 26.2 eV). This is exploited, to take EFTEM images at different energy losses (Fig. 7a-c) to reveal the distribution of FHBC and PC₆₁BM. The hatched rectangles in Fig. 7d mark the corresponding energy loss windows which were selected with a slit width of 4 eV. The EFTEM image Fig. 7a was taken with a slit position centered at an energy loss of 20 eV. For this energy loss the FHBC signal distinctly exceeds the PC₆₁BM signal leading to a higher image intensity of the FHBC-rich regions. For the second slit position centered at 23 eV, the two signals have the same intensity, and changes of the image contrast in Fig. 7b can be interpreted in terms of thickness variations. The last slit position centered at 27 eV exhibits a higher PC₆₁BM signal. The PC₆₁BM-rich phase appears brighter in the EFTEM image Fig. 7c. This image closely resembles the PC₆₁BM-sensitive DF TEM image (Fig. 4d), in which the PC₆₁BM also appears brighter than the FHBC. The comparison of Fig. 7a and Fig. 7b shows complementary contrast indicating that small FHBC precipitates are embedded in a PC₆₁BM:FHBC blend.

TEM tomography was applied to analyze the 3D structure of the sample. In Fig. 8 three slices extracted from the top (Fig. 8a), center (Fig. 8b) and bottom (Fig. 8c) of the reconstructed volume are shown. FHBC-rich regions appear dark because the image contrast was inverted for improved visibility. The dark FHBC precipitates are distributed homogeneously over the whole sample thickness, but seem to be slightly larger close to the bottom of the sample (Fig. 8c). Fig. 8a shows a slice close to the sample surface, where bright structures are visible in the upper right corner (marked with arrows). They correspond to the faint elongated structures in the AFM images (Fig. 3a and Fig. 4a) which surround the depressions. By applying a threshold

gray value to the reconstructed volume, the FHBC domains could be extracted and a 3D-model of the FHBC distribution was obtained (see video in the supplementary information). The video confirms that the FHBC domains are homogeneously distributed over the whole volume of the sample.

GIWAXS was performed to study the crystalline organization of the FHBC:PC₆₁BM sample after annealing at 150 °C for up to 120 s. The GIWAXS pattern of the sample before annealing (not presented here) does not exhibit any reflections, indicating none or very poor order on a macroscopic scale (few cm²) in the probed volume. Fig. 9a shows the GIWAXS pattern of a pure FHBC sample which was processed in the same way as the FHBC:PC₆₁BM blend. Three discrete reflections can be recognized in the meridional and off-meridional planes which are characteristic for a hexagonal organization of the columnar stacks with their columnar axes oriented parallel to the surface as illustrated in Fig. 9c. The respective distance between the FHBC stack layers corresponds to $d = 2.22$ nm which agrees well with the lattice fringe distance of 2.15 nm in the HRTEM image of the FHBC:PC₆₁BM blend after annealing (Fig. 6). Due to the low crystalline order on a macroscopic scale, only the 1st order reflections appear without higher order reflections. Reflections from the FHBC π - π stacking are not observed because The GIWAXS pattern of the FHBC:PC₆₁BM blend (sample annealed for 120 s at 150 °C) (Fig. 9b) resembles the GIWAXS pattern of pure FHBC (Fig. 9a). However, the azimuthal intensity distribution of the main reflection indicate a decrease of order if PC₆₁BM is added (comparison of insets of Fig. 9a and b). This can be inferred from the smearing out of the reflections along the azimuthal angle in the inset of Fig. 9b, while these reflections are quite sharp for of pure FHBC (inset of Fig. 9a).

Discussion

Detailed information on the nanomorphology of the FHBC:PC₆₁BM absorber layers and the effect of annealing was obtained by combining several electron microscopic techniques, AFM and GIWAXS. We first focus on the nanomorphology of the FHBC:PC₆₁BM blend before annealing. The images and SAED pattern in Fig. 3 demonstrate that the non-annealed sample consists of a homogeneous mixture of PC₆₁BM and FHBC stacks. The FHBC stack axes are preferentially oriented parallel to the substrate with an additional azimuthal texture in regions with a typical size between a few 100 nm and 1 μ m. The PC₆₁BM molecules are homogeneously distributed and do not agglomerate to form, e.g., pure PC₆₁BM crystallites. This is illustrated in Fig. 10a where a scheme of the nanomorphology of the non-annealed FHBC:PC₆₁BM sample is shown.

The morphology of the annealed samples is schematically summarized in Fig. 10b. The most notable change of the nanomorphology after annealing consists in the precipitation of crystalline FHBC as demonstrated by the DF TEM (Fig. 4c, Fig. 5b-d), HRTEM (Fig. 6) and the GIWAXS data (Fig. 9). The FHBC stacks are arranged in a hexagonal symmetry as indicated in Fig. 1c and Fig. 9c. The GIWAXS data confirm that the stack axes in the precipitates are indeed preferentially oriented parallel to the substrate (Fig. 9b). PC₆₁BM-sensitive EFTEM (Fig. 7c) and DF TEM images (Fig. 4d) reveal a homogeneous distribution of the PC₆₁BM molecules. Furthermore the FHBC-sensitive DF TEM images (Fig. 4c and Fig. 5b-d) show that the surrounding PC₆₁BM:FHBC blend contains regions with preferentially aligned FHBC stacks as the non-annealed sample. The size of these regions does not change with increasing annealing time. In contrast, the pure FHBC precipitates grow slightly with increasing annealing time, which becomes apparent in the FHBC-sensitive DF TEM images of the annealing series in Fig. 5. The growth of the FHBC precipitates leads to an FHBC depletion of the surrounding FHBC:PC₆₁BM blend. For long annealing times (5 min), large PC₆₁BM precipitates are formed which may be initiated by the FHBC depletion of the FHBC:PC₆₁BM blend. The precipitation of large PC₆₁BM crystals has been observed before for long annealing times and high PC₆₁BM concentrations in other PC₆₁BM-based absorber layer blends, e.g., in P3HT:PC₆₁BM blends^{22, 24}.

Electron tomography (Fig. 8, and supplementary information) reveals that the FHBC precipitates are homogeneously distributed over the entire sample volume. However, the FHBC precipitate size is slightly larger close to the bottom of the layer which indicates that FHBC precipitation is slightly favored at the interface to the PEDOT:PSS. The annealing process induces only minor changes of the surface topography. The AFM image of the annealed sample (Fig. 4a) exhibits the same 10 nm deep depressions as the image of the non-annealed sample (Fig. 3a). Only the large-scale thickness variations are reduced.

The nanomorphology of the FHBC:PC₆₁BM blends can be correlated with the photovoltaic performance of the respective solar cells. Annealing of the active layer is required to substantially improve the device power conversion efficiency. The J-V characteristic of the non-annealed device shows a pronounced S-shape. S-shapes are often attributed to unbalanced hole and electron charge carrier extraction rates. Accordingly, we assume that the intimate mixing of the blend's donor and acceptor component, as illustrated in Fig. 10a, disables continuous percolation pathways and hence causes a similar effect. Thermal annealing of the active layer leads to the precipitation of crystalline FHBC, and improves the interfacial contact between the different layers in the BHJ. These interface changes can lead to enhanced charge

extraction and carrier mobility, and therefore enhance the device performance. The samples annealed for 20 s and 40 s exhibit the best PCE of 1.31 % and 1.35 %, respectively. This indicates that the absorber layer is sensitive towards small changes of the FHBC precipitate size. An intermediate size of the crystalline FHBC precipitates (obtained after 20 and 40 s of annealing at 150 °C), surrounded by a homogenous mixture of FHBC stacks and PC₆₁BM, yields the best exciton dissociation and charge transport among the studied samples. Nevertheless, the PCE of the cells is not particularly high which can be ascribed to the fact that the FHBC stacks are oriented “edge-on” parallel to the substrate plane. This orientation is unfavorable for charge transport which preferentially occurs along the FHBC stack axis. Additionally, the insulation side chains of the FHBC molecules impede the charge transport perpendicular to the substrate. A more favorable organization of the FHBC columns would be “face-on”, where the columns are oriented perpendicular to the absorber layer. This orientation would support efficient charge carrier transport to the electrodes.

Summary

The nanomorphology and power conversion efficiency of FHBC:PC₆₁BM-based BHJ OSCs was studied and correlated before and after annealing at 150 °C for up to 120 s. FHBC is an interesting donor material for OSCs due to the high fill factor of the solar cells and the possibility for further derivatisation. The application of several electron microscopic techniques, AFM and GIWAXS revealed the complex nanomorphology of the FHBC:PC₆₁BM layers and its dependence on the annealing treatment.

The results of the study can be summarized as follows:

- Due to π - π stacking, the FHBC molecules assemble into columnar stacks with a distance of 0.35 nm between the FHBC molecules. FHBC stacks are already present before annealing.
- The non-annealed sample consists of a mixture of homogeneously distributed PC₆₁BM molecules and FHBC stacks with a preferential in-plane stack orientation (texture). Strongly textured regions with the same FHBC stack orientation have sizes between a few 100 nm and 1 μ m.
- During annealing, FHBC crystallites are precipitated from the FHBC:PC₆₁BM mixture. They exhibit the same crystalline structure like pure FHBC, namely a hexagonal arrangement of the FHCB stacks, with a lattice plane distance of 2.15 nm.

- The FHBC precipitates grow with increasing annealing time until the depletion of the FHBC in the mixed phase reaches a critical value and large PC₆₁BM crystals are formed.
- The FHBC precipitates are distributed homogeneously over the whole volume of the absorber layer as shown by electron tomography. The size of the FHBC precipitates is larger close to the bottom of the layer probably due to preferential FHBC nucleation at the PEDOT:PSS interface.
- The best solar cell efficiencies were obtained for samples annealed for 20 s and 40 s. This annealing time yields the best phase separation between donor and acceptor material.

So far, the weak absorption and the orientation of the FHBC stacks parallel to the substrate (edge-on) enable moderate PCEs only. However, depending on future smart molecule and device design and hence improved absorption and charge carrier transport properties, FHBC will be a promising material class for self-organizing bulk heterojunction solar cells.

Materials and Methods

Materials:

The synthesis of 2,11-bis(9,9-dioctyl-9H-fluoren-2-yl)hexabenzob[bc,ef,hi,kl,no,qr]coronene (FHBC) has been reported previously.^{19, 25} PC₆₁BM (99.5 %) was purchased from Solenne BV.

Solar cell fabrication:

Bulk-heterojunction (BHJ) solar cells were fabricated by spin coating of 30-nm-thick layers of PEDOT:PSS; Baytron AI 4083 from HC Starck) on patterned glass/ITO substrates which were cleaned by acetone, and 2-propanol in an ultrasonication bath and UV/ozone-treated. The PEDOT:PSS films were baked at 140 °C for 10 min in air. A blend of FHBC and PC₆₁BM with a ratio of 1:2 was then spin coated from chlorobenzene solution with a thickness of about 75 nm. A TiO_x precursor solution (1:200 in methanol) was deposited on the active layer by spin coating (2000 rpm) to form a TiO_x layer with a thickness of about 10 nm. The films were exposed to air for about 20 min at room temperature for hydrolysis or baked at 150 °C for 20 s, 40 s, 60 s and 120 s. The films were transferred to a evaporation chamber where aluminum

(100 nm) was deposited through a shadow mask (active area: 0.06 cm²) at approximately 1x10⁻⁶ torr. Film thicknesses were determined by Veeco Dektak 150+ Surface Profiler. Current density-voltage (J-V) measurements were carried out with a Keithley 2400 source measurement unit under AM1.5G (1000 W/m²) illumination from an Oriel solar simulator. The illumination intensity was calibrated using a reference silicon solar cell (PVmeasurements Inc.) certified by the National Renewable Energy Laboratory. Device fabrication and characterizations were performed in an ambient environment without any encapsulation.

For the GIWAXS investigations samples without electrode were prepared.

Sample preparation for electron microscopy investigations:

Samples without top electrode were prepared under inert conditions for the nanomorphology studies. The PEDOT:PSS layer thickness was slightly increased (~45 nm) to facilitate the dissolution of the layer for TEM sample preparation. The samples were annealed at 150 °C for 20-120 s and 300 s.

Plan-view samples of the photoactive layers were prepared by the following procedure. First, the absorbing layer on the substrate was cut with a scalpel into small pieces. As PEDOT:PSS is water soluble, the pieces of the active layer can be floated off the substrate by a drop of water from where they can be transferred onto conventional TEM copper grids. The sample thickness was about 90 nm for all samples as determined by focused-ion-beam cross sections.

Electron Microscopy:

TEM images and diffraction patterns were recorded with a Philips CM200 FEG/ST at 200 keV. The EELS, EFTEM and tomography analysis were performed in an FEI TITAN³ 80-300 at 300 keV. EELS and EFTEM were performed with a Gatan Tridiem 865 HR imaging filter. EEL spectra were recorded with an energy resolution of 0.7 eV and a dispersion 0.05 eV/pixel. 1000 spectra with an exposure time of 0.01 s were acquired and summed up. For the EFTEM images the exposure time was 4 s, and an energy slit width of 4 eV was chosen.

For tomography, a tilt series of bright-field TEM images was acquired in a tilt-angle range of ±77° in steps of 1° with a "Fischione Model 2020" tomography sample holder, resulting in 155 images. For the tilt series acquisition the software package 'FEI Xplore 3D' was used. Subsequent alignment of the image stack and reconstruction of the tomogram were performed with the 'FEI Inspect3D V3.0' software. The reconstruction of the tomogram is based on the SIRT algorithm²⁶ which was performed with 20 iterations. A sectioning of the tomogram's

inner structure was obtained by applying a grey-level threshold to the image stack to distinguish between FHBC and PC₆₁BM regions. The ‘Amira/ResolveRT’ software was then used to convert the tomogram into a 3D model.

AFM and GIWAXS:

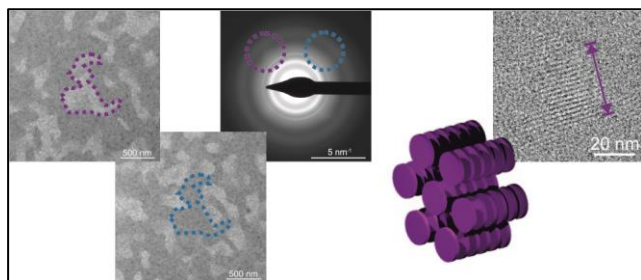
AFM topography images were taken with an Asylum Research MFP-3D in the AC mode.

GIWAXS measurements were performed using a custom setup consisting of rotating anode X-ray source (Rigaku Micromax, operated at 42 kV and 20 mA), Osmic confocal MaxFlux optics and a three pin-hole collimation system (JJ X-ray). Samples on the top of approx. 1×1 cm silicon platelets were irradiated at the incident angle (α_i) of 0.20°. Diffraction patterns were recorded on a MAR345 image plate detector.

ACKNOWLEDGMENT

This work has been performed within the project F1 of the DFG Research Center for Functional Nanostructures (CFN). It has been further supported by a grant from the Ministry of Science, Research and the Arts of Baden-Württemberg (Az: 7713.14–300). M. F. G. Klein is supported by the Karlsruhe School of Optics and Photonics (KSOP). This work is also supported by the Australian Solar Institute (project grant 1-GER001 and Fellowship for W. W. H. Wong), the Victorian Organic Solar Cell Consortium (www.vicosc.unimelb.edu.au), the Victorian State Government Department of Business Innovation (Victorian Science Agenda) and Department of Primary Industries (Energy Technology Innovation Strategy), the AAS-BMBF Australia-Germany Solar Photovoltaic Research Exchange Program. Special thanks are given to Professor Andrew Holmes for generous support of this project. Adam Kiersnowski acknowledges the funding through the statutory subsidy from the Polish Ministry of Science and Higher Education for the Faculty of Chemistry of Wroclaw University of Technology.

TOC IMAGE The author must submit a graphic in the actual size to be used for the TOC that will fit in an area 1.4 in. high and 3.3 in. wide (3.6 cm × 8.4 cm).



REFERENCES (with Endnote!)

1. Krebs, F. C.; Tromholt, T.; Jorgensen, M., Upscaling of polymer solar cell fabrication using full roll-to-roll processing. *Nanoscale* **2010**, *2*, 873-886.
2. Brabec, C. J.; Gowrisanker, S.; Halls, J. J. M.; Laird, D.; Jia, S.; Williams, S. P., Polymer–Fullerene Bulk-Heterojunction Solar Cells. *Adv. Mater.* **2010**, *22*, 3839-3856.
3. Günes, S.; Neugebauer, H.; Sariciftci, N. S., Conjugated Polymer-Based Organic Solar Cells. *Chem. Rev.* **2007**, *107*, 1324-1338.
4. Liu, F.; Gu, Y.; Jung, J. W.; Jo, W. H.; Russell, T. P., On the morphology of polymer-based photovoltaics. *Journal of Polymer Science Part B: Polymer Physics* **2012**, *50*, 1018-1044.
5. Bertho, S.; Oosterbaan, W. D.; Vrindts, V.; D'Haen, J.; Cleij, T. J.; Lutsen, L.; Manca, J.; Vanderzande, D., Controlling the morphology of nanofiber-P3HT:PCBM blends for organic bulk heterojunction solar cells. *Organic Electronics* **2009**, *10*, 1248-1251.
6. Savenije, T. J.; Kroeze, J. E.; Yang, X.; Loos, J., The formation of crystalline P3HT fibrils upon annealing of a PCBM:P3HT bulk heterojunction. *Thin Solid Films* **2006**, *511-512*, 2-6.
7. Vanlaeke, P.; Swinnen, A.; Haeldermans, I.; Vanhoyland, G.; Aernouts, T.; Cheyns, D.; Deibel, C.; D'Haen, J.; Heremans, P., *et al.*, P3HT/PCBM bulk heterojunction solar cells: Relation between morphology and electro-optical characteristics. *Solar Energy Materials and Solar Cells* **2006**, *90*, 2150-2158.
8. Zhang, X.; Hudson, S. D.; DeLongchamp, D. M.; Gundlach, D. J.; Heeney, M.; McCulloch, I., In-Plane Liquid Crystalline Texture of High-Performance Thienothiophene Copolymer Thin Films. *Advanced Functional Materials* **2010**, *20*, 4098-4106.
9. Petermann, J.; Moritz, H.; Rieck, U.; Wood, B. A.; Thomas, E. L., A novel TEM dark-field contrast method for semi-crystalline polymers. *J Mater Sci Lett* **1989**, *8*, 1023-1025.
10. Martin, D. C.; Chen, J.; Yang, J.; Drummy, L. F.; Kübel, C., High resolution electron microscopy of ordered polymers and organic molecular crystals: Recent developments and future possibilities. *Journal of Polymer Science Part B: Polymer Physics* **2005**, *43*, 1749-1778.
11. Drummy, L. F.; Davis, R. J.; Moore, D. L.; Durstock, M.; Vaia, R. A.; Hsu, J. W. P., Molecular-Scale and Nanoscale Morphology of P3HT:PCBM Bulk Heterojunctions: Energy-Filtered TEM and Low-Dose HREM. *Chemistry of Materials* **2010**, *23*, 907-912.
12. Herzing, A. A.; Richter, L. J.; Anderson, I. M., 3D Nanoscale Characterization of Thin-Film Organic Photovoltaic Device Structures via Spectroscopic Contrast in the TEM. *Journal of Physical Chemistry C* **2010**, *114*, 17501-17508.

13. Pfannmöller, M.; Flügge, H.; Benner, G.; Wacker, I.; Sommer, C.; Hanselmann, M.; Schmale, S.; Schmidt, H.; Hamprecht, F. A., *et al.*, Visualizing a Homogeneous Blend in Bulk Heterojunction Polymer Solar Cells by Analytical Electron Microscopy. *Nano Letters* **2011**, *11*, 3099-3107.
14. Pfaff, M.; Klein, M. F. G.; Müller, E.; Müller, P.; Colsmann, A.; Lemmer, U.; Gerthsen, D., Nanomorphology of P3HT:PCBM-Based Absorber Layers of Organic Solar Cells after Different Processing Conditions Analyzed by Low-Energy Scanning Transmission Electron Microscopy. *Microscopy and Microanalysis* **2012**, *18*, 1380-1388.
15. van Bavel, S. S.; Sourty, E.; de With, G.; Loos, J., Three-Dimensional Nanoscale Organization of Bulk Heterojunction Polymer Solar Cells. *Nano Letters* **2009**, *9*, 507-513.
16. van Bavel, S. S.; Bärenklau, M.; de With, G.; Hoppe, H.; Loos, J., P3HT/PCBM Bulk Heterojunction Solar Cells: Impact of Blend Composition and 3D Morphology on Device Performance. *Advanced Functional Materials* **2010**, *20*, 1458-1463.
17. Andersson, B. V.; Masich, S.; Solin, N.; Inganäs, O., Morphology of organic electronic materials imaged via electron tomography. *Journal of Microscopy* **2012**, *247*, 277-287.
18. Roehling, J. D.; Batenburg, K. J.; Swain, F. B.; Moulé, A. J.; Arslan, I., Three-Dimensional Concentration Mapping of Organic Blends. *Advanced Functional Materials* **2012**, n/a-n/a.
19. Wong, W. W. H.; Singh, T. B.; Vak, D.; Pisula, W.; Yan, C.; Feng, X.; Williams, E. L.; Chan, K. L.; Mao, Q., *et al.*, Solution Processable Fluorenyl Hexa-peri-hexabenzocoronenes in Organic Field-Effect Transistors and Solar Cells. *Advanced Functional Materials* **2010**, *20*, 927-938.
20. Schmidt-Mende, L.; Fechtenkötter, A.; Müllen, K.; Moons, E.; Friend, R. H.; MacKenzie, J. D., Self-organized discotic liquid crystals for high-efficiency organic photovoltaics. *Science* **2001**, *293*, 1119-1122.
21. Singh, T. B.; Chen, X.; Wong, W. H.; Ehlig, T.; Kemppinen, P.; Chen, M.; Watkins, S.; Winzenberg, K.; Holdcroft, S., *et al.*, Correlation of charge extraction properties and short circuit current in various organic binary and ternary blend photovoltaic devices. *Appl. Phys. A* **2012**, *108*, 515-520.
22. Swinnen, A.; Haeldermans, I.; Vanlaeke, P.; D'Haen, J.; Poortmans, J.; D'Oliessaer, M.; Manca, J. V., Dual crystallization behaviour of polythiophene/fullerene blends. *The European Physical Journal - Applied Physics* **2006**, *36*, 251-256.
23. Ma, W. L.; Yang, C. Y.; Gong, X.; Lee, K.; Heeger, A. J., Thermally stable, efficient polymer solar cells with nanoscale control of the interpenetrating network morphology. *Advanced Functional Materials* **2005**, *15*, 1617-1622.

24. Swinnen, A.; Haeldermans, I.; vande Ven, M.; D'Haen, J.; Vanhoyland, G.; Aresu, S.; D'Olieslaeger, M.; Manca, J., Tuning the Dimensions of C60-Based Needlelike Crystals in Blended Thin Films. *Advanced Functional Materials* **2006**, *16*, 760-765.
25. Jones, D. J.; Purushothaman, B.; Ji, S.; Holmes, A. B.; Wong, W. W. H., Synthesis of electron-poor hexa-peri-hexabenzocoronenes. *Chemical Communications* **2012**, *48*, 8066-8068.
26. Gilbert, P., Iterative methods for the three-dimensional reconstruction of an object from projections. *Journal of Theoretical Biology* **1972**, *36*, 105-117.
27. Wong, W. W. H.; Ma, C.-Q.; Pisula, W.; Mavrinskiy, A.; Feng, X.; Seyler, H.; Jones, D. J.; Müllen, K.; Bäuerle, P., *et al.*, Fluorenyl Hexa-peri-hexabenzocoronene-Dendritic Oligothiophene Hybrid Materials: Synthesis, Photophysical Properties, Self-Association Behaviour and Device Performance. *Chemistry – A European Journal* **2011**, *17*, 5549-5560.

TABLES

Table 1. Photovoltaic performance of FHBC:PC₆₁BM solar cells depending on various annealing times.

Annealing time [s]	J _{sc} [mA/cm ²]	V _{oc} [V]	FF [%]	PCE [%]
0	1.96	0.93	33	0.58
20	2.86	0.92	51	1.35
40	2.93	0.90	50	1.31
60	2.47	0.86	45	0.96
120	2.19	0.82	37	0.66

FIGURES

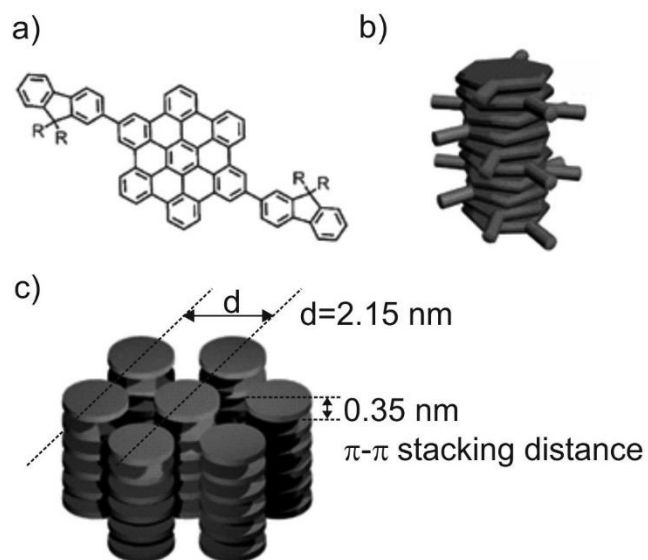


Fig. 1. a) Chemical structure of the FHBC molecule, b) schematic column of stacked FHBC molecules,¹⁹ c) hexagonal arrangement of the columnar stacks.²⁷

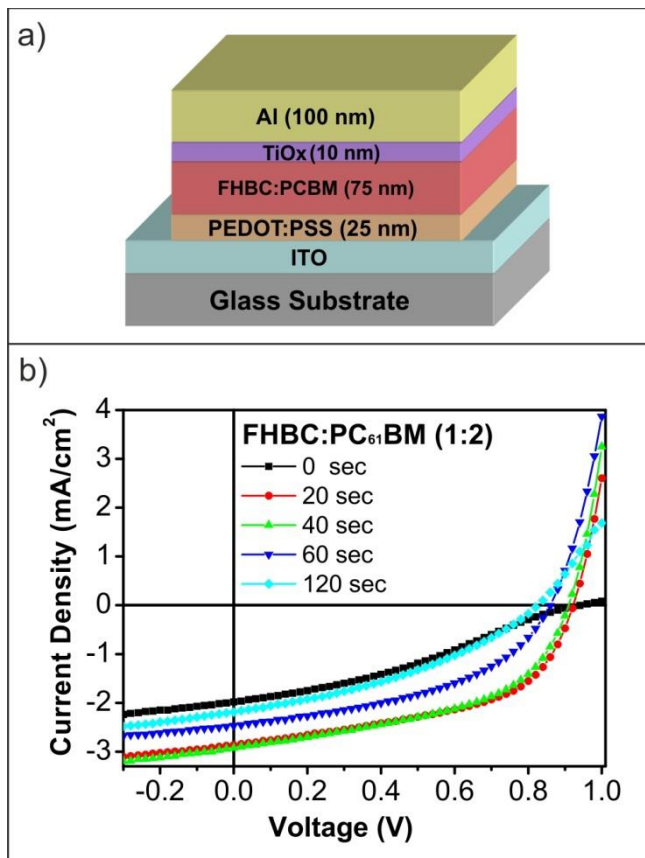


Fig. 2. Schematic diagram of the organic solar cells with regular device geometry and (b) J-V characteristics of the FHBC:PC₆₁BM based BHJ solar cells with different annealing times under AM 1.5 G solar illumination, 1000 W/m².

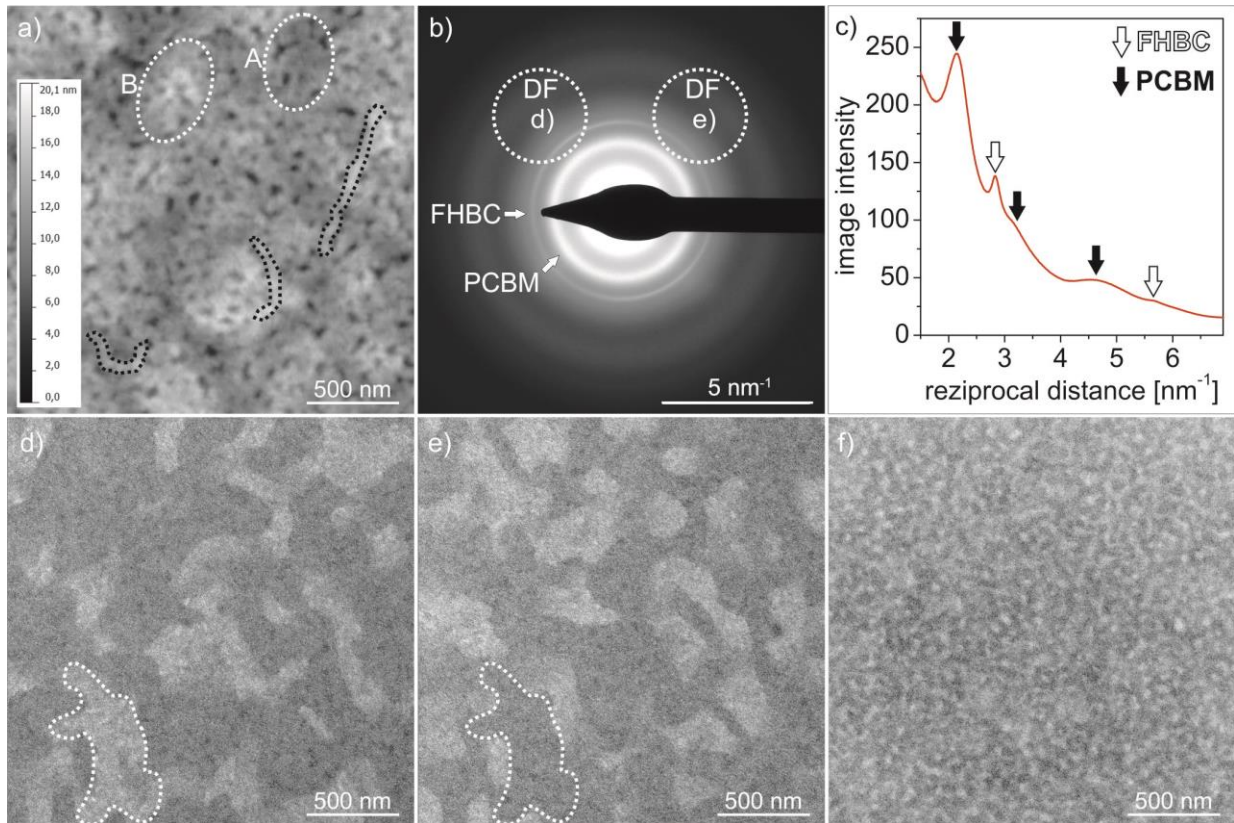


Fig. 3. Nanomorphology of the non-annealed FHBC:PC₆₁BM sample. a) AFM topography image. The dashed white circles mark a deeper (A) and a higher (B) region of the sample. The dashed black lines mark elongated surface structures. b) TEM diffraction pattern and aperture positions for the DF images (dashed circles); c) radial linescan of the diffraction pattern; d) and e) FHBC-sensitive DF TEM images taken at 200 keV corresponding to the aperture positions marked in the diffraction pattern. One grain, which shows contrast inversion, is exemplarily marked in both images. f) BF TEM image of the same sample position.

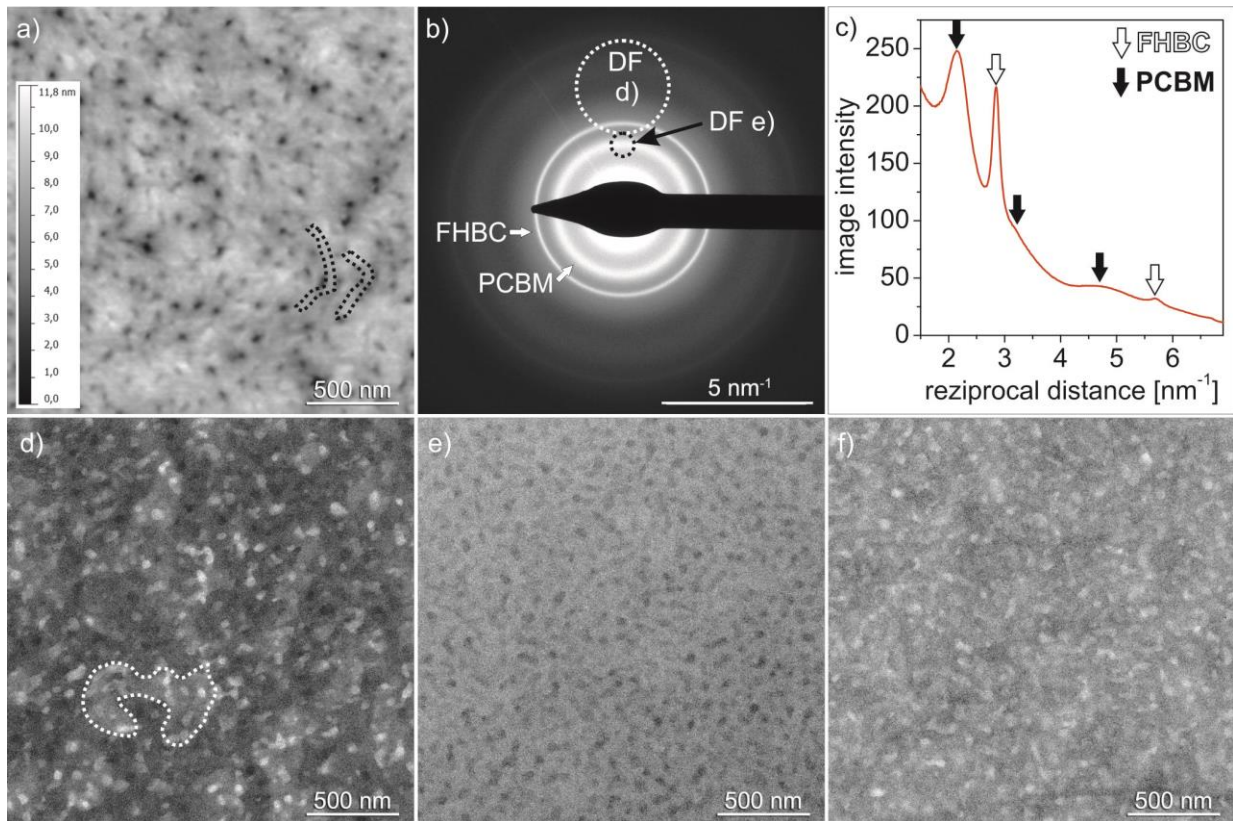


Fig. 4. Nanomorphology of the FHBC:PC₆₁BM sample annealed for 120 s. a) AFM topography image. The dashed black lines mark elongated surface structures; b) TEM diffraction pattern and aperture positions for the DF images (dashed circles); c) radial linescan of the diffraction pattern; d) DF TEM image taken at 200 keV corresponding to the aperture position on the FHBC ring (marked in b)). One grain with the same preferential orientation of the FHBC stacks is marked; e) DF image corresponding to the aperture position on the PC₆₁BM ring (also marked in b)) of another sample position; f) BF TEM image taken at the same sample position as the PC₆₁BM-sensitive DF image.

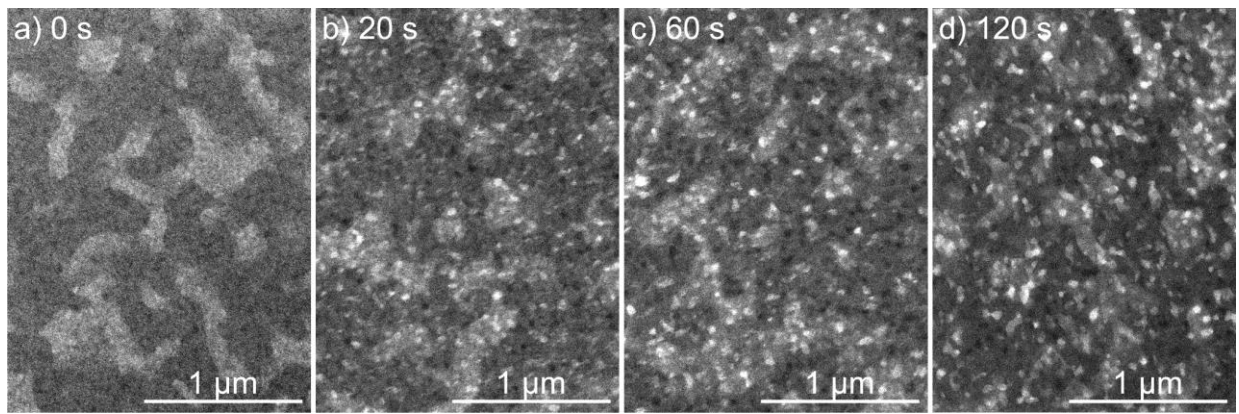


Fig. 5. FHBC-sensitive DF TEM images of samples annealed for a) 0, b) 20, c) 60 and d) 120 s.

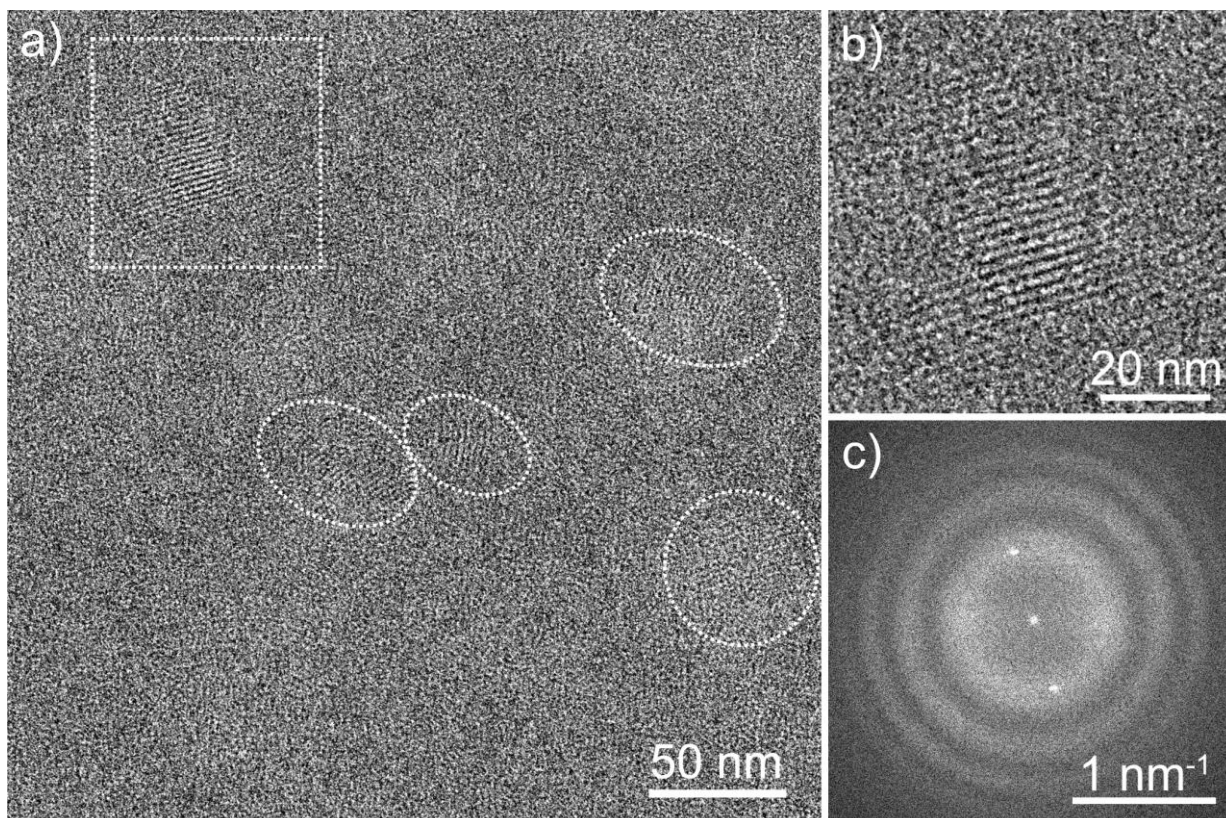


Fig. 6. a) 200 keV HRTEM image of the FHBC:PC₆₁BM sample annealed for 60 s. Crystalline regions are encircled, b) enlarged image of the dashed square in the HRTEM image, c) Fourier transform of HRTEM image.

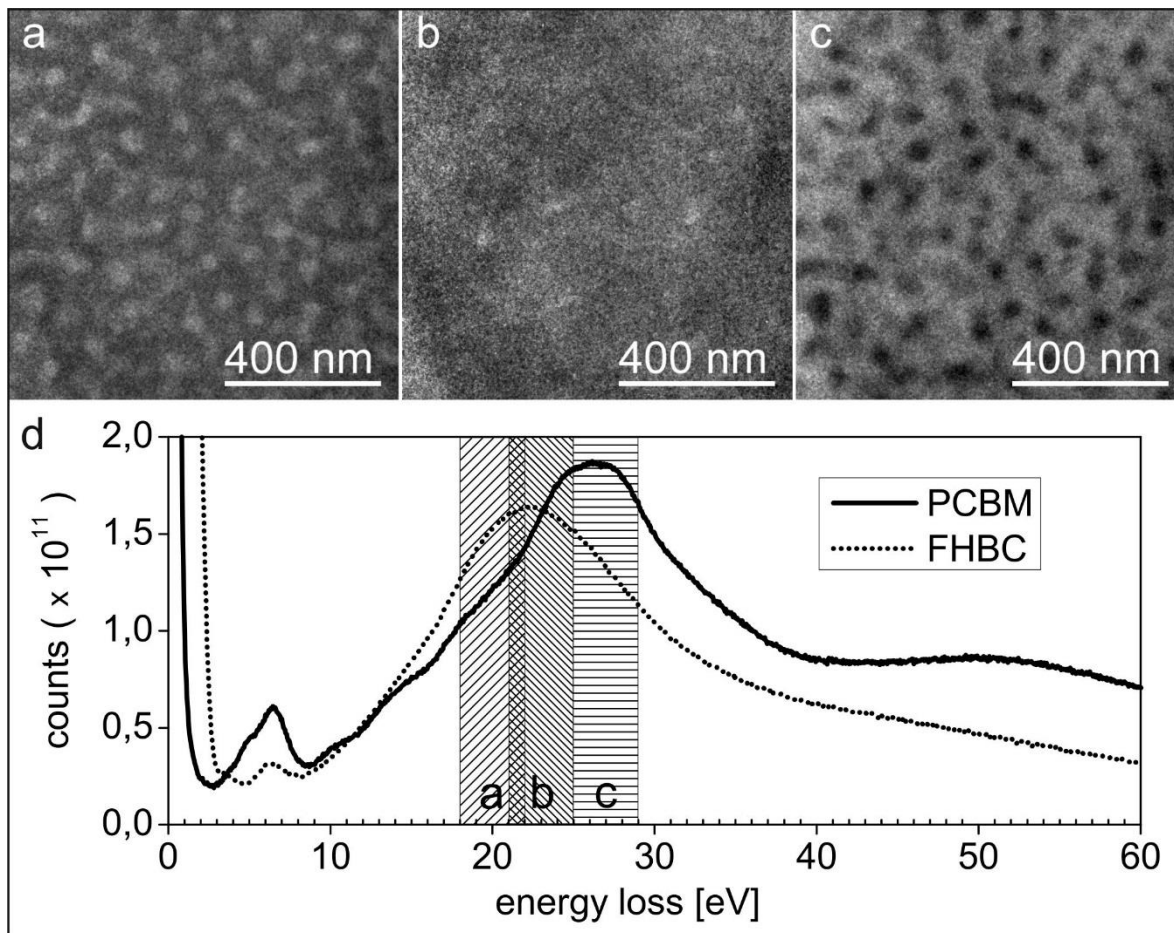


Fig. 7. EFTEM images of the FHBC:PC₆₁BM sample annelaed for 60 s. The images are taken with a slit width of 4 eV centered at energy losses of a) 20 eV, b) 23 eV and c) 27 eV. d) Low-loss EEL sprectra of pure PC₆₁BM and FHBC. The slit positions for the EFTEM images are marked by the hatched rectangles.

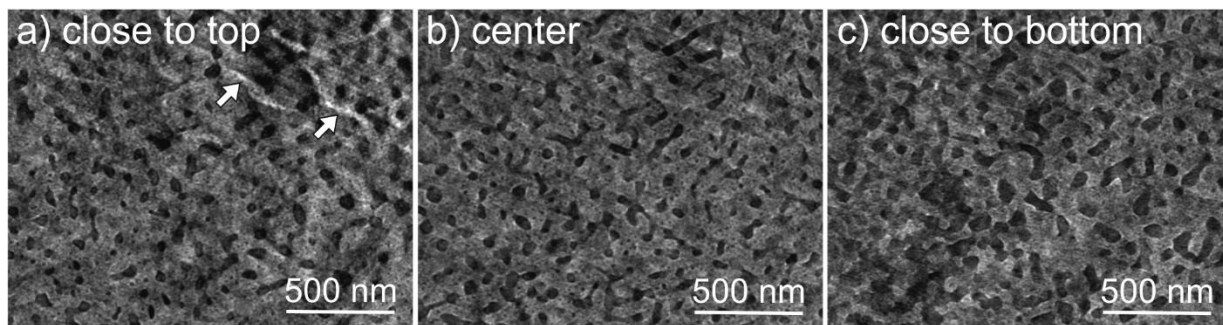


Fig. 8. Slices extracted from the TEM tomogram of the sample annealed for 60 s. FHBC precipitates appear dark because the contrast is inverted for better visibility. a) Slice close to the top, b) slice from the center and c) slice close to the bottom of the sample. The white arrows in a) indicate elongated surface structures.

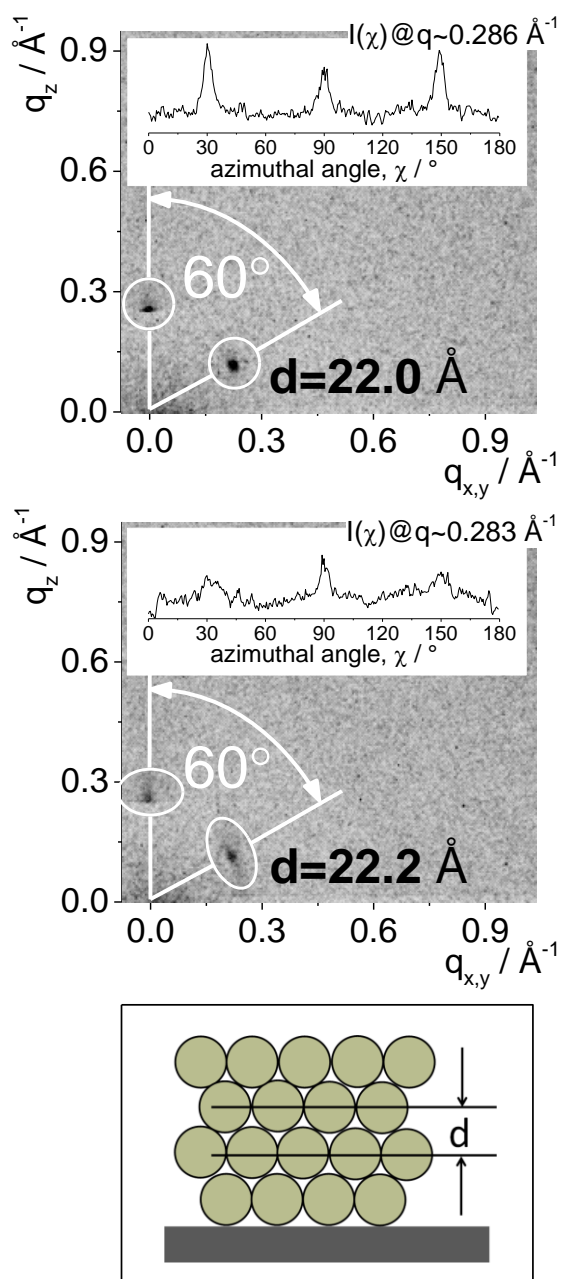


Fig. 9. GIWAXS patterns of a) pure FHBC and b) FHBC:PC₆₁BM blend after annealing at 150 °C for 120 s with indicated azimuthal angle and d-spacing. Insets show the azimuthal intensity distributions ($I(\chi)$) at the scattering vectors (q) corresponding to reflections of the hexagonal structure, c) schematic illustration of the hexagonal arrangement of FHBC stacks on the surface.

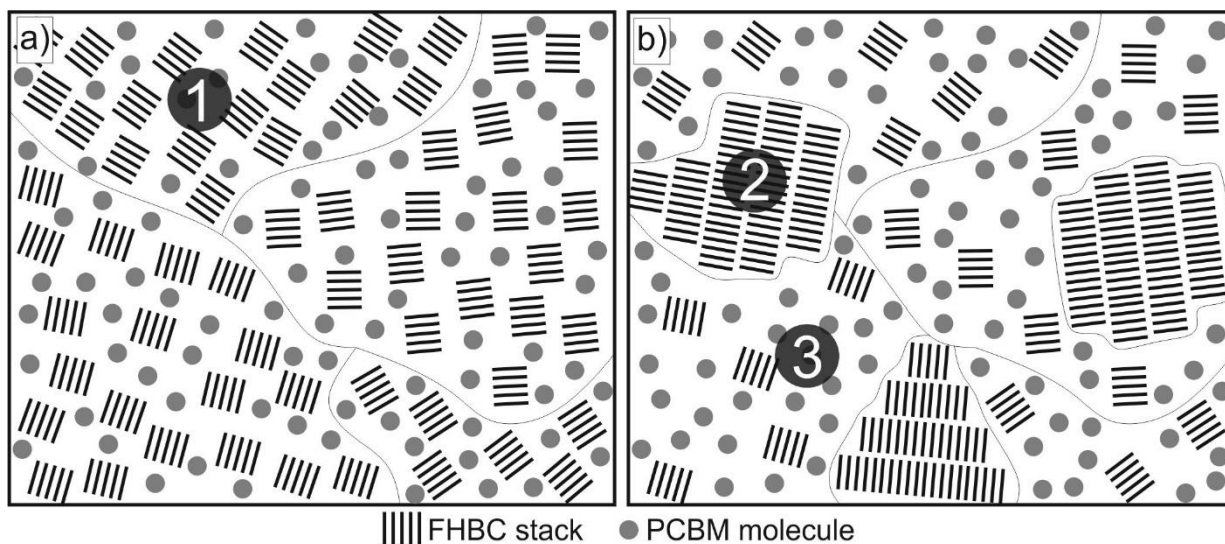


Fig. 10. Schematic illustration of the nanomorphology of a) non-annealed and b) annealed FHBC:PC₆₁BM. Before annealing, the sample consists of a homogeneous mixture of FHBC and PC₆₁BM. Grains (1) exist with FHBC stacks which are preferentially aligned parallel to the substrate. During annealing FHBC crystals are precipitated (2) from the textured FHBC:PC₆₁BM mixture (3).